

Article

Optimizing the Synthetic Conditions of “Green” Colloidal AgBiS₂ Nanocrystals Using a Low-Cost Sulfur Source

Qiao Li ¹, Xiaosong Zheng ¹, Xiaoyu Shen ¹, Shuai Ding ¹, Hongjian Feng ^{1,*}, Guohua Wu ^{2,*}
and Yaohong Zhang ^{1,3,*} 

¹ School of Physics, Northwest University, Xi’an 710127, China

² Qingdao Innovation and Development Base of Harbin Engineering University, Harbin Engineering University, Harbin 150001, China

³ Shaanxi Key Laboratory for Carbon Neutral Technology, Xi’an 710127, China

* Correspondence: hjfeng@nwu.edu.cn (H.F.); ghwu@hrbeu.edu.cn (G.W.); yhzhang@nwu.edu.cn (Y.Z.)

Abstract: Colloidal AgBiS₂ nanocrystals (NCs) have attracted increasing attention as a near-infrared absorbent materials with non-toxic elements and a high absorption coefficient. In recent years, colloidal AgBiS₂ NCs have typically been synthesized via the hot injection method using hexamethyldisilathiane (TMS) as the sulfur source. However, the cost of TMS is one of the biggest obstacles to large-scale synthesis of colloidal AgBiS₂ NCs. Herein, we synthesized colloidal AgBiS₂ NCs using oleylamine@sulfur (OLA-S) solution as the sulfur source instead of TMS and optimized the synthesis conditions of colloidal AgBiS₂ NCs. By controlling the reaction injection temperature and the dosage of OLA-S, colloidal AgBiS₂ NCs with adjustable size can be synthesized. Compared with TMS-based colloidal AgBiS₂ NCs, the colloidal AgBiS₂ NCs based on OLA-S has good crystallinity and fewer defects.

Keywords: AgBiS₂; colloidal nanocrystals; hot injection; sulfur source



Citation: Li, Q.; Zheng, X.; Shen, X.; Ding, S.; Feng, H.; Wu, G.; Zhang, Y. Optimizing the Synthetic Conditions of “Green” Colloidal AgBiS₂ Nanocrystals Using a Low-Cost Sulfur Source. *Nanomaterials* **2022**, *12*, 3742. <https://doi.org/10.3390/nano12213742>

Academic Editor: Efrat Lifshitz

Received: 23 September 2022

Accepted: 21 October 2022

Published: 25 October 2022

Publisher’s Note: MDPI stays neutral with regard to jurisdictional claims in published maps and institutional affiliations.



Copyright: © 2022 by the authors. Licensee MDPI, Basel, Switzerland. This article is an open access article distributed under the terms and conditions of the Creative Commons Attribution (CC BY) license (<https://creativecommons.org/licenses/by/4.0/>).

1. Introduction

Colloidal AgBiS₂ nanocrystal (NC), a member of the I–V–VI₂ ternary semiconductor materials [1–7], is a promising eco-friendly material for solar cells owing to colloidal AgBiS₂ NC having a wide absorption spectrum in the visible to near-infrared region (300–1600 nm) [8–10], high absorption coefficient ($\sim 10^5$ cm^{−1}) [1,11–13], and good air stability [8]. The hot injection method is widely used to prepare high quality NCs such as PbS [14], PbSe [15,16], and halide perovskite NCs [17–22]. In 2016, Bernechea et al. synthesized colloidal AgBiS₂ NCs by the hot injection method using hexamethyldisilathiane (TMS) as the sulfur source and first reported colloidal AgBiS₂ NC-based solar cells with a certified power conversion efficiency (PCE) of 6.3% [1]. Subsequently, colloidal AgBiS₂ NC-based solar cells have gradually become one of the mainstays of new generation solar cells. Subsequently, Hu et al. synthesized colloidal AgBiS₂ NCs using an improved amine-based synthesis route, improving the PCE of colloidal AgBiS₂ NC-based solar cells by 30% using colloidal AgBiS₂ NCs synthesized using a modified route [23]. Oh et al. improved the size distribution of colloidal AgBiS₂ NCs by an optimized synthetic route, resulting in enhanced photovoltaic performance [24]. Akgul et al. synthesized colloidal AgBiS₂ NCs at room temperature using an improved sulfur amine-based synthesis route, reducing the production price by 60% and achieving a PCE of 5.5% [25]. These results demonstrate that the quality of colloidal AgBiS₂ NCs plays an important role in the performance of solar cells. Therefore, it is of extreme importance to synthesize monodispersed colloidal AgBiS₂ NCs in the quantum confinement regime and with a high phase purity [26]. Yet, it should be noted that although synthesis of colloidal AgBiS₂ NCs has been developed by several researchers [1,27–30], it remains challenging to synthesize colloidal AgBiS₂ NCs with a perfect crystal structure and complete elimination of defects [31–38]. Furthermore,

using expensive and unstable TMS as the sulfur source in colloidal AgBiS₂ NCs synthesis process results in high cost of the synthesis reaction, which is not conducive to large-scale preparation of colloidal AgBiS₂ NC. It is urgent to explore a method to synthesize high quality colloidal AgBiS₂ NC with low cost.

As a cheap sulfur source, oleylamine@sulfur (OLA-S) solution has been widely used to synthesize high quality CdS [39], ZnS [40], and PbS NCs [41,42]. Moreover, as a ligand stabilizer, oleylamine can passivate the surface defects of NCs and regulate their growth [23,43]. Recently, Nakazawa et al. successfully synthesized colloidal AgBiS₂ NCs with OLA-S as sulfur source [44]. However, the effect of OLA-S on the growth and quality of colloidal AgBiS₂ NCs has not been studied in detail. In this work, in order to improve the quality of colloidal AgBiS₂ NCs and reduce the preparation cost, we synthesized colloidal AgBiS₂ NCs by hot injection method and using OLA-S as the sulfur source to replace TMS, then investigated the effect of OLA-S on the growth of colloidal AgBiS₂ NCs. By regulating the dosage of OLA-S, high quality colloidal AgBiS₂ NCs with low defect density and uniform size were prepared. It was found that the size of colloidal AgBiS₂ NCs could be controlled by changing the reaction injection temperature. Compared with TMS-based colloidal AgBiS₂ NCs, the colloidal AgBiS₂ NCs based on OLA-S have good crystallinity and fewer defects. In addition, the synthesis cost is significantly reduced.

2. Materials and Methods

Chemicals and materials. Bismuth (III) acetate (Bi(OAc)₃, 99.9%, Aladdin, China), silver acetate (AgOAc, 99.5%, Aladdin, China), oleic acid (OA, 90%, Sigma-Aldrich, USA), hexamethyldisilathiane (TMS, synthesis grade, Sigma-Aldrich, Switzerland), 1-Octadecene (ODE, 90%, Aladdin, China), oleylamine (OLA, 80–90%, Aladdin, China), sulfur (S, 99.5%, Sinopharm, China), acetone (99.5%, Sinopharm, China), toluene (99.5%, Sinopharm, China), hexane(97.0%, Sinopharm, China).

Synthesis of TMS-based colloidal AgBiS₂ NCs. The TMS-based colloidal AgBiS₂ NCs were synthesized following a hot injection method reported previously in the literature [29].

Synthesis of OLA-S-based colloidal AgBiS₂ NCs. The synthesis of OLA-S-based colloidal AgBiS₂ NCs was carried out similarly to that of TMS-based colloidal AgBiS₂ NCs. The OLA-S (1 M) solution was prepared by dissolving sulfur powder in OLA solution at room temperature. To investigate the influence of the reaction injection temperature (80 °C, 100 °C, 120 °C) on synthesis of OLA-S-based colloidal AgBiS₂ NCs, the dosage of OLA-S solution (1 M) was kept at 3 mL. In contrast, to investigate the influence of the dosage of OLA-S solution (1 mL, 2 mL, 3 mL and 4 mL) on synthesis of OLA-S-based colloidal AgBiS₂ NCs, the reaction injection temperature was kept at 100 °C. After rapidly injected the OLA-S solution into the cationic solution, heating was stopped while stirring was maintained until the reaction solution cooled to room temperature. The colloidal AgBiS₂ NCs were collected using an acetone/toluene solvent system in air, and the obtained colloidal AgBiS₂ NCs precipitate was then dried in a vacuum drying oven at room temperature. Finally, the colloidal AgBiS₂ NCs were dispersed in hexane solution.

Characterization

The phase identification of colloidal AgBiS₂ NCs was carried out using powder X-ray diffraction (XRD, Bruker, D8 ADVANCED, Germany). The morphology and crystal structure of the prepared colloidal AgBiS₂ NCs were characterized using high-resolution transmission electron microscopy (HR-TEM, Thermo Fisher Scientific, Talos F200x, USA). The TEM samples were prepared as follows: the obtained colloidal AgBiS₂ NCs were dispersed in hexane with a concentration of 2 mg/mL, three drops of the mixture solution were dropped onto the TEM support film via pipette gun, and the TEM support films were fully dried in the vacuum drying oven before measurement. The acceleration voltage of electron beam was 200 KV during the TEM test. Elemental mapping of the colloidal AgBiS₂ NCs was carried out using a TEM equipped with an energy dispersive spectrometer (EDS). UV-vis-NIR absorption spectra of the colloidal AgBiS₂ NCs were recorded with a

spectrophotometer (Shimadzu, UV-3600 PLUS, Japan). Fourier transform-infrared spectra (FT-IR) of colloidal AgBiS₂ NCs were recorded using an infrared spectrometer (Bruker, INVENIO, Germany). The photoluminescent (PL) spectra of the colloidal AgBiS₂ NCs were measured by using a fluorescence spectrophotometer (Zolix instruments Co., Ltd, FST1-MPL303-OP1, Beijing, China).

3. Results and Discussion

Following the schematic diagram of the synthesis of colloidal AgBiS₂ NCs by hot injection method, which is shown in Figure 1, we adopted two methods to synthesize colloidal AgBiS₂ NCs using TMS (path 1) and OLA-S (path 2) as the sulfur source. The variation of the crystal structure and phase of TMS-based and OLA-S-based colloidal AgBiS₂ NCs were studied using X-ray diffraction (XRD). Figure 2a shows the XRD patterns of the TMS-based and OLA-S-based colloidal AgBiS₂ NCs (dosage of OLA-S: 3 mL, injection temperature: 100 °C). For both samples, six XRD peaks are found at 13.75°, 15.85°, 22.89°, 27.12°, 28.20°, and 33.11°, which can be assigned to the facets (111), (200), (220), (311), (222), and (400) of AgBiS₂ cubic rock salt structure (JCPDS No. 21-1178), respectively [8,12,37,45–47]. This indicates that colloidal AgBiS₂ NCs can be successfully prepared by using OLA-S as the sulfur source. For NC materials, the broadening of XRD peaks can be roughly attributed to the size effect of NCs and lattice strain, which is closely related to defects in the NCs [48]. The lattice strains in TMS-based and OLA-S-based colloidal AgBiS₂ NCs were calculated using the Williams–Hall plot method [49], with the results shown in Figure S1 and the corresponding Table S1. The obtained values of the lattice strains for TMS-based and OLA-S-based colloidal AgBiS₂ NCs are 0.33 and 0.27, respectively. It can be seen that the lattice strain for TMS-based colloidal AgBiS₂ NCs is larger than that of the OLA-S-based NCs, with the larger lattice strain leading to more defects in the NCs. Thus, the results demonstrate that OLA-S-based colloidal AgBiS₂ NCs have lower defect density than TMS-based NCs. In other words, as a new sulfur source, OLA-S can be used to synthesize high quality colloidal AgBiS₂ NCs.

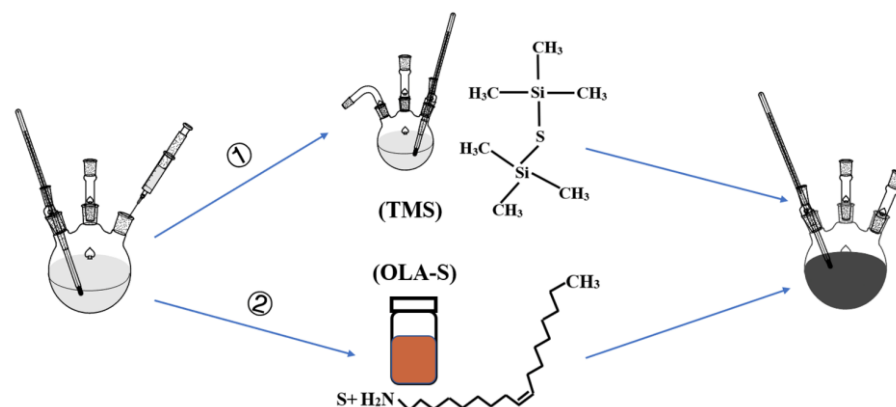


Figure 1. Synthetic route for colloidal AgBiS₂ NCs using different sulfur sources (path 1: TMS, path 2: OLA-S).

Furthermore, in order to reveal the influence of the sulfur source on the morphology and size distribution of colloidal AgBiS₂ NCs, transmission electron microscopy (TEM) measurement was carried out. Figure S2 shows that colloidal AgBiS₂ NCs prepared using TMS and OLA-S have a uniform spherical shape. The average diameters of TMS-based and OLA-S-based colloidal AgBiS₂ NCs are about 4.3 ± 1.6 nm (Figure S2a) and 7.8 ± 1.9 nm (Figure S2b), respectively. High-resolution TEM (HR-TEM) images of spherical colloidal AgBiS₂ NCs based on TMS and OLA-S are shown in Figure 2b,c [50–52]. Lattice spacing of about 0.32 nm, corresponding to (111) crystal plane spacing of cubic rock salt structure AgBiS₂, can be clearly seen, which is consistent with the XRD results above. Elemental mapping of TMS-based colloidal AgBiS₂ NCs was carried out using a TEM equipped with EDS. Elemental mapping images are provided in Figure S3a–c, where the Ag, Bi, and S

elements are distributed throughout all NCs. Moreover, the atomic percentages of Ag, Bi, and S elements are 41.3, 22.3, and 36.4, respectively. These results indicate that the surface of TMS-based colloidal AgBiS₂ NCs should be silver-rich and sulfur-poor. Figure S3d–f shows the element mapping images of OLA-S-based colloidal AgBiS₂ NCs. The atomic percentages of Ag, Bi, and S elements are 42.6, 12.3, and 45.1, respectively. This means that the surface of OLA-S-based colloidal AgBiS₂ NCs is both silver-rich and sulfur-rich. Combined with the XRD result of the OLA-S-based colloidal AgBiS₂ NCs, the signal of Ag₂S is not observed in Figure 2a. Therefore, we speculate that the excess Ag and S are coating on the surface of colloidal AgBiS₂ NCs rather than forming Ag₂S impurities.

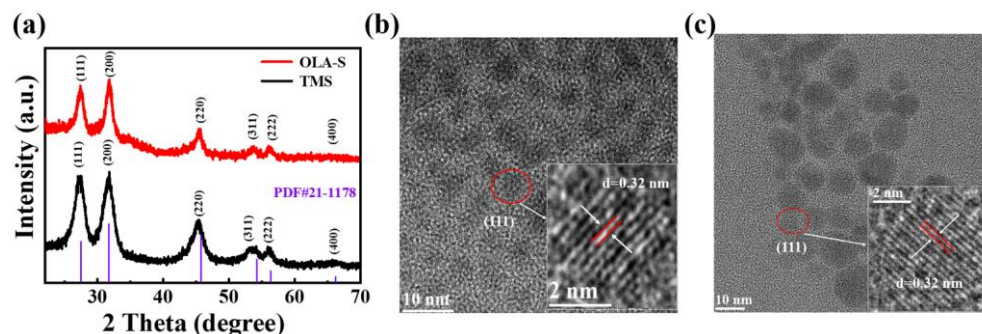


Figure 2. (a) XRD patterns of colloidal AgBiS₂ NCs based on TMS and OLA-S; (b,c) HR-TEM images of TMS-based and OLA-S-based colloidal AgBiS₂ NCs, respectively.

To further reveal the effect of the sulfur source on the quality of the obtained colloidal AgBiS₂ NCs, the photoluminescent (PL) spectra of the TMS-based and OLA-S-based colloidal AgBiS₂ NCs solutions were measured at room temperature [53]. The PL spectra of colloidal AgBiS₂ NCs based on TMS and OLA-S are shown in Figure 3a. We detected PL signals in the emission range of 400–1000 nm using a 330 nm excitation wavelength. It can be seen that the PL intensity of OLA-S-based colloidal AgBiS₂ NCs is stronger than that of TMS-based colloidal AgBiS₂ NCs under the same concentration. This indicates that there are fewer nonradiative charge recombination centers, which is closely related to lower defect density, in the OLA-S-based colloidal AgBiS₂ NCs compared to the TMS-based colloidal AgBiS₂ NCs.

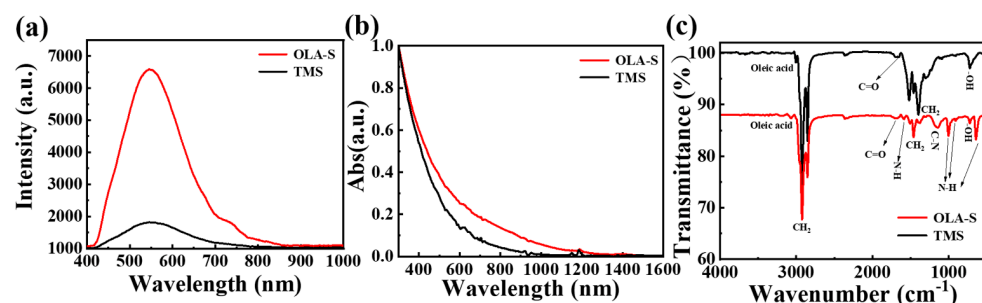


Figure 3. (a) PL spectra of TMS-based and OLA-S-based colloidal AgBiS₂ NCs, (b) UV-vis-NIR absorption spectra of the colloidal AgBiS₂ NCs in hexane, and (c) FT-IR spectra of colloidal AgBiS₂ NCs.

The UV-vis-NIR absorption spectra of TMS-based and OLA-S-based colloidal AgBiS₂ NCs are shown in Figure 3b. It can be seen that the absorption spectra of both of TMS-based and OLA-S-based colloidal AgBiS₂ NCs do not exhibit any exciton absorption peak or sharp absorption edge in the range of 300–1600 nm, which is similar to the previously reported colloidal AgBiS₂ NCs and other ternary semiconductor NCs such as colloidal CuInS₂, AgInS₂ and AgBiSe₂ NCs [6,54–56]. The absorption spectrum of OLA-S-based colloidal AgBiS₂ NCs extends to a larger IR region than the TMS-based colloidal AgBiS₂ NCs, which may be owing to the size effect of larger grain size of OLA-S-based colloidal AgBiS₂ NCs. This result is consistent with the result of the TEM images shown above.

FT-IR spectroscopy was employed to investigate the functional groups on the obtained colloidal AgBiS₂ NCs [44,57]. Figure 3c shows the FT-IR spectra of colloidal AgBiS₂ NCs. For TMS-based colloidal AgBiS₂ NCs, the =C-H stretching peak at 3006 cm⁻¹, C-H absorption stretching peaks at 2961, 2929, and 2854 cm⁻¹, and C=O stretching mode at 1678 cm⁻¹ are assigned to OA ligands on the surface of colloidal AgBiS₂ NCs [55,58]. For OLA-S-based colloidal AgBiS₂ NCs, the peaks at 903 cm⁻¹, 721 cm⁻¹, and 641 cm⁻¹ are attributed to N-H vibrations of OLA. Additionally, a C-N stretching mode peak was observed at 1145 cm⁻¹. The peak at 1678 cm⁻¹ can be assigned to C=O stretching of OA ligands, indicating that the OLA-S-based colloidal AgBiS₂ NCs are coated by OLA and OA ligands and that there are no amide-type ligands on the surface of the colloidal AgBiS₂ NCs.

In order to reveal the influence of reaction temperature on the synthesis of OLA-S-based colloidal AgBiS₂ NCs, a synthetic experiment was carried out at 80 °C, 100 °C, and 120 °C. The crystal structure and phase transition of colloidal AgBiS₂ NCs based on OLA-S were investigated using XRD. Figure 4a shows the XRD patterns of OLA-S-based colloidal AgBiS₂ NCs which were synthesized under different injection temperatures. The results show that colloidal AgBiS₂ NCs can be successfully prepared at 100 °C and 120 °C. For sample prepared at 80 °C, the weak diffraction peak intensity indicates poor crystallinity of the obtained product and there are peaks belonging to monoclinic structure Ag₂S (JCPDS No. 14-0072) at which impurities can be found. Therefore, pure colloidal AgBiS₂ NCs cannot be synthesized at low temperature when using OLA-S as the sulfur source. The lattice strains of OLA-S-based colloidal AgBiS₂ NCs obtained at 100 °C and 120 °C were calculated using the Williams-Hall plot from Figure S4, the corresponding results are shown in Table S2. The values of the lattice strains for OLA-S-based colloidal AgBiS₂ NCs prepared at 100 °C and 120 °C are 0.27 and 0.38, respectively. It can be seen that the lattice strain of OLA-S-based colloidal AgBiS₂ NCs produced at 120 °C is greater than the lattice strain OLA-S-based colloidal AgBiS₂ NCs prepared at 100 °C, with larger lattice strain leading to more defects in the NCs. These results show that the defect density OLA-S-based colloidal AgBiS₂ NCs prepared at 100 °C was lower than that of OLA-S-based NCs produced at 120 °C, meaning that 100 °C can be used to synthesize high quality colloidal AgBiS₂ NC.

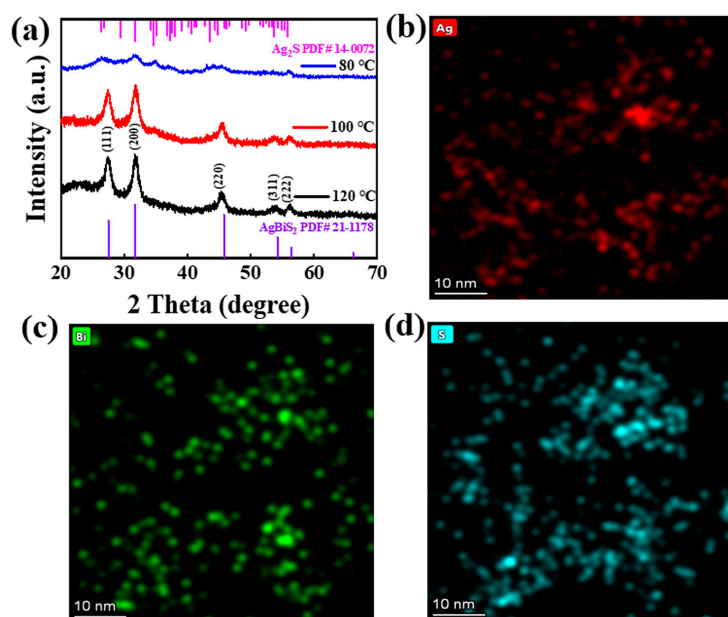
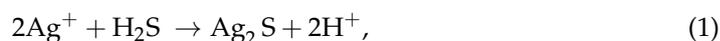


Figure 4. (a) XRD patterns of OLA-S-based colloidal AgBiS₂ NCs synthesized at 80 °C, 100 °C, and 120 °C; (b–d) EDS elemental mapping (TEM) images of OLA-S-based colloidal AgBiS₂ NCs prepared at 120 °C.

TEM measurement was used to reveal the influence of reaction temperature on the morphology and size distribution of OLA-S-based colloidal AgBiS₂ NCs. Figure S5 shows that the colloidal AgBiS₂ NCs prepared at 120 °C have a uniform spherical shape and that the average diameter of the obtained NCs is 12.1 ± 3.5 nm (Figure S5a). An HR-TEM image of colloidal AgBiS₂ NCs prepared at 120 °C is shown in Figure S5b. The cubic rock salt structure of AgBiS₂ with a lattice spacing of about 0.32 nm corresponding to the (111) crystal plane spacing can be seen, and is consistent with the XRD results. Figure 4b–d provides elemental diagram images of OLA-S-based colloidal AgBiS₂ NCs synthesized at 120 °C. The atomic percentages of Ag, Bi, and S are 48.4, 17.1, and 34.6, respectively. These results show that the surface of the obtained colloidal AgBiS₂ NCs should be silver-rich and sulfur-rich. Because the lattice strain of the OLA-S-based colloidal AgBiS₂ NCs prepared at 120 °C is larger than that prepared at 100 °C, high reaction temperature may be detrimental to the preparation of high quality OLA-S-based colloidal AgBiS₂ NCs.

Figure S6a shows the UV-vis-NIR absorption spectra of OLA-S-based colloidal AgBiS₂ NCs prepared at 100 °C and 120 °C. The absorption spectrum of the sample synthesized at 120 °C extends to more IR regions than that of the NCs prepared at 100 °C, which is mainly caused by the size effect of the colloidal AgBiS₂ NCs. To further reveal the effect of reaction injection temperature on the quality of the obtained colloidal AgBiS₂ NCs, the PL spectra of OLA-S-based colloidal AgBiS₂ NCs prepared at 100 °C and 120 °C were measured using 330 nm excitation wavelength at room temperature. The PL intensity of OLA-S-based colloidal AgBiS₂ NCs synthesized at 100 °C is stronger than that of NCs synthesized at 120 °C (Figure S6b). This reflects that the OLA-S-based colloidal AgBiS₂ NCs prepared at 100 °C has fewer defects than the colloidal AgBiS₂ NCs synthesized at 120 °C.

In addition, the influence of OLA-S dosage in the reaction when synthesizing colloidal AgBiS₂ NCs was investigated. We carried out the synthesis of colloidal AgBiS₂ NCs using different amount of OLA-S (1 M). The crystallinity and phase purity of OLA-S-based colloidal AgBiS₂ NCs synthesized under different conditions were examined by XRD. (Figure 5). It can be seen that only Ag₂S was produced in the reaction when using 1 mL OLA-S, while both Ag₂S and AgBiS₂ were formed when the dosage of OLA-S was increased to 2 mL. Thus, pure phase colloidal AgBiS₂ NCs can be successfully prepared using 3 mL and 4 mL OLA-S. Based on these results, we speculate that the reaction process of OLA-S-based colloidal AgBiS₂ NC synthesis should be that: H₂S being released in situ from OLA-S after OLA-S was injected into high temperature cationic solution [59], and then reacting with Ag⁺ to form Ag₂S, subsequently, the produced Ag₂S reacts with Bi³⁺ to form AgBiS₂ NCs. The reaction equations are as follows:



The lattice strain values calculated for the colloidal AgBiS₂ NCs prepared by using 3 mL and 4 mL OLA-S are 0.27 and 0.40, respectively, as shown in Figure S7 and Table S3. The smaller lattice strain in colloidal AgBiS₂ NCs prepared using 3 mL OLA-S indicates a lower defect density in the NCs. To clarify the effect of the dosage of OLA-S on the morphology and size distribution of colloidal AgBiS₂ NCs, we carried out HR-TEM measurements of the obtained AgBiS₂ NCs. Figure S8a shows that colloidal AgBiS₂ NCs prepared using 4 mL OLA-S have a uniform spherical shape and the average diameters of NCs are about 8.3 ± 2.7 nm, which is a little larger than that based on 3 mL OLA-S (7.8 ± 1.9 nm; see Figure S2b). Figure S6c shows the UV-vis-NIR absorption spectra of 3 mL and 4 mL OLA-S-based colloidal AgBiS₂ NCs. The absorption spectrum of the 4 mL OLA-S-based colloidal AgBiS₂ NCs extends to more IR regions than that of the 3 mL OLA-S-based colloidal AgBiS₂ NCs, which is mainly caused by the size effect of the colloidal AgBiS₂ NCs.

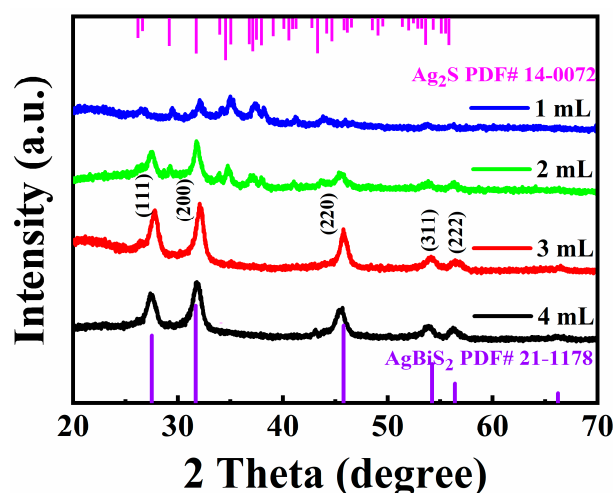


Figure 5. XRD patterns of colloidal OLA-S-based AgBiS₂ NCs using 1 mL, 2 mL, 3 mL, and 4 mL.

Finally, we calculated the cost and yield of the synthesis of colloidal AgBiS₂ NCs using TMS and OLA-S as sulfur sources. Compared with TMS, the cost of synthesis using OLA-S was reduced about 57% (see Table S4 for details). We found that the yield of colloidal AgBiS₂ NCs based on TMS and OLA-S were 86.9% and 90.5%, respectively. This indicates that OLA-S can replace TMS for synthesizing colloidal AgBiS₂ NCs as a low-cost sulfur source.

4. Conclusions

In summary, we optimized the synthesis conditions of colloidal AgBiS₂ NCs using OLA-S as the sulfur source. Colloidal AgBiS₂ NCs with high quality and pure phase can be synthesized by rationally optimizing the dosage and reaction injection temperature of OLA-S. Compared with TMS as the sulfur source, OLA-S-based colloidal AgBiS₂ NCs have lower defect density and a wider absorption spectrum. More importantly, the cost of synthesis is greatly reduced, as the yield of colloidal AgBiS₂ NCs is increased when using OLA-S to replace the more expensive TMS. In addition, the pungent odor and air sensitivity of TMS can be avoided. As a low-cost sulfur source, OLA-S has the potential to for use in synthesizing other sulfide NCs in the future.

Supplementary Materials: The supporting information can be downloaded at: <https://www.mdpi.com/article/10.3390/nano12213742/s1>. Figure S1. The William-Hall plots for (a) TMS-based and (b) OLA-S-based colloidal AgBiS₂ NCs. Figure S2. TEM images of (a) TMS-based and (b) OLA-S-based colloidal AgBiS₂ NCs. Insets are the statistical histograms of the NCs size distribution. SAED images of (c) TMS-based and (d) OLA-S-based colloidal AgBiS₂ NCs. Figure S3. EDS-Mapping images of (a), (b) and (c) TMS-based. EDS-Mapping images of (d), (e) and (f) OLA-S-based colloidal AgBiS₂ NCs. Figure S4. The William-Hall plots for (a) and (b) OLA-S-based colloidal AgBiS₂ NCs prepare at 100 °C and 120 °C. Figure S5. TEM images of (a) OLA-S-based colloidal AgBiS₂ NCs prepare at 120 °C. Insets are the statistical histograms of the NCs size distribution. (b) HR-TEM images of OLA-S-based colloidal AgBiS₂ NCs prepare at 120 °C. (c) SAED image of OLA-S-based colloidal AgBiS₂ NCs prepare at 120 °C. Figure S6. (a) UV-vis-NIR absorption spectra of the colloidal AgBiS₂ NCs in hexane. (b) PL spectrum and fitting curves of OLA-S-based colloidal AgBiS₂ NCs prepare at 100 °C and 120 °C. (b) UV-vis-NIR absorption spectra of the 3 mL and 4 mL colloidal AgBiS₂ NCs in hexane. Figure S7. The William-Hall plots for (a) 3 mL and (b) 4 mL OLA-S-based colloidal AgBiS₂ NCs. Figure S8. TEM images of (a) 4 mL OLA-S-based colloidal AgBiS₂ NCs. Insets are the statistical histograms of the NCs size distribution. (b) HR-TEM images of 4 mL OLA-S-based colloidal AgBiS₂ NCs. (c) SAED image of 4 mL OLA-S-based colloidal AgBiS₂ NCs. Table S1. Half-peak widths and lattice strains of OLA-S-based and TMS-based colloidal AgBiS₂ NCs. Table S2. Half-peak widths and lattice strains of OLA-S-based colloidal AgBiS₂ NCs prepare at 100 °C and 120 °C. Table S3. Half-peak widths and lattice strains of 3 mL and 4 mL OLA-S-based colloidal

AgBiS₂ NCs. Table S4. Raw material usage, price and yield of AgBiS₂ NCs based on TMS and OLA-S. Reference [60] is cited in the Supplementary Materials.

Author Contributions: Q.L. and Y.Z. conceived and designed the experiments; Q.L., X.Z., X.S. and S.D. performed the experiments; Q.L., X.Z. and Y.Z. analyzed the data; H.F., G.W. and Y.Z. contributed reagents/materials/analysis tools; Q.L. wrote the paper; Y.Z. and G.W. corrected the paper. All authors have read and agreed to the published version of the manuscript.

Funding: This research was supported by the National Natural Science Foundation of China under grant No. 52103223.

Data Availability Statement: The data that support the findings of this study are available from the corresponding author upon reasonable request.

Conflicts of Interest: The authors declare no conflict of interest.

References

- Bernechea, M.; Miller, N.C.; Xercavins, G.; So, D.; Stavrinadis, A.; Konstantatos, G. Solution-processed solar cells based on environmentally friendly AgBiS₂ nanocrystals. *Nat. Photon.* **2016**, *10*, 521–525. [[CrossRef](#)]
- Liu, Y.; Cadavid, D.; Ibanez, M.; De Roo, J.; Ortega, S.; Dobrozhan, O.; Kovalenko, M.V.; Cabot, A. Colloidal AgSbSe₂ nanocrystals: Surface analysis, electronic doping and processing into thermoelectric nanomaterials. *J. Mater. Chem. C* **2016**, *4*, 4756–4762. [[CrossRef](#)]
- Liu, Y.; Garcia, G.; Ortega, S.; Cadavid, D.; Palacios, P.; Lu, J.; Ibanez, M.; Xi, L.; De Roo, J.; Lopez, A.M.; et al. Solution-based synthesis and processing of Sn- and Bi-doped Cu₃SbSe₄ nanocrystals, nanomaterials and ring-shaped thermoelectric generators. *J. Mater. Chem. A* **2017**, *5*, 2592–2602. [[CrossRef](#)]
- Zhou, B.; Li, M.; Wu, Y.; Yang, C.; Zhang, W.H.; Li, C. Monodisperse AgSbS₂ nanocrystals: Size-control strategy, large-scale synthesis, and photoelectrochemistry. *Chem. Eur. J.* **2015**, *21*, 11143–11151. [[CrossRef](#)] [[PubMed](#)]
- Guria, A.K.; Prusty, G.; Chacrabarty, S.; Pradhan, N. Fixed aspect ratio rod-to-rod conversion and localized surface plasmon resonance in semiconducting I-V-VI nanorods. *Adv. Mater.* **2016**, *28*, 447–453. [[CrossRef](#)] [[PubMed](#)]
- Kuznetsova, V.; Tkach, A.; Cherevko, S.; Sokolova, A.; Gromova, Y.; Osipova, V.; Baranov, M.; Ugolkov, V.; Fedorov, A.; Baranov, A. Spectral-time multiplexing in FRET complexes of AgInS₂/ZnS quantum dot and organic dyes. *Nanomaterials* **2020**, *10*, 1569. [[CrossRef](#)]
- Bai, X.; Purcell-Milton, F.; Gun'ko, Y.K. Optical properties, Synthesis, and potential applications of Cu-Based ternary or quaternary anisotropic quantum dots, polytypic nanocrystals, and core/shell heterostructures. *Nanomaterials* **2019**, *9*, 85. [[CrossRef](#)]
- Pejova, B.; Nesheva, D.; Aneva, Z.; Petrova, A. Photoconductivity and relaxation dynamics in sonochemically synthesized assemblies of AgBiS₂ quantum dots. *J. Mater. Chem. C* **2011**, *115*, 37–46. [[CrossRef](#)]
- Smith, A.M.; Duan, H.; Rhyner, M.N.; Ruan, G.; Nie, S. A systematic examination of surface coatings on the optical and chemical properties of semiconductor quantum dots. *Phys. Chem. Chem. Phys.* **2006**, *8*, 3895–3903. [[CrossRef](#)]
- Do, S.; Kwon, W.; Rhee, S.W. Soft-template synthesis of nitrogen-doped carbon nanodots: Tunable visible-light photoluminescence and phosphor-based light-emitting diodes. *J. Mater. Chem. C* **2014**, *2*, 4221–4226. [[CrossRef](#)]
- Vines, F.; Bernechea, M.; Konstantatos, G.; Illas, F. Matildite versus schapbachite: First-principles investigation of the origin of photoactivity in AgBiS₂. *Phys. Rev. B* **2016**, *94*, 235203. [[CrossRef](#)]
- Hameed, T.A.; Wassel, A.R.; El Radaf, I.M. Investigating the effect of thickness on the structural, morphological, optical and electrical properties of AgBiSe₂ thin films. *J. Alloys Compd.* **2019**, *805*, 1–11. [[CrossRef](#)]
- Zhou, S.; Yang, J.; Li, W.; Jiang, Q.; Luo, Y.; Zhang, D.; Zhou, Z.; Li, X. Preparation and photovoltaic properties of ternary AgBiS₂ quantum dots sensitized TiO₂ nanorods photoanodes by electrochemical atomic layer deposition. *J. Electrochem. Soc.* **2016**, *163*, D63–D67. [[CrossRef](#)]
- Zhang, Y.H.; Wu, G.H.; Ding, C.; Liu, F.; Liu, D.; Masuda, T.; Yoshino, K.; Hayase, S.; Wang, R.X.; Shen, Q. Surface-modified graphene oxide/lead sulfide hybrid film-forming ink for high-efficiency bulk nano-heterojunction colloidal quantum dot solar cells. *Nano Micro Lett.* **2020**, *12*, 111. [[CrossRef](#)]
- Zhang, Y.H.; Wu, G.H.; Ding, C.; Liu, F.; Yao, Y.F.; Zhou, Y.; Wu, C.P.; Nakazawa, N.; Huang, Q.X.; Toyoda, T.; et al. Lead selenide colloidal quantum dot solar cells achieving high open-circuit voltage with one-step deposition strategy. *J. Phys. Chem. Lett.* **2018**, *9*, 3598–3603. [[CrossRef](#)]
- Zhang, Y.H.; Ding, C.; Wu, G.H.; Nakazawa, N.; Chang, J.; Ogomi, Y.; Toyoda, T.; Hayase, S.; Katayama, K.; Shen, Q. Air stable PbSe colloidal quantum dot heterojunction solar cells: Ligand-dependent exciton dissociation, recombination, photovoltaic property, and stability. *J. Phys. Chem. C* **2016**, *120*, 28509–28518. [[CrossRef](#)]
- Wang, X.C.; Bai, T.X.; Yang, B.; Zhang, R.L.; Zheng, D.Y.; Jiang, J.K.; Tao, S.X.; Liu, F.; Han, K.L. Germanium halides serving as ideal precursors: Designing a more effective and less toxic route to high-optoelectronic-quality metal halide perovskite nanocrystals. *Nano Lett.* **2022**, *22*, 636–643. [[CrossRef](#)]

18. Wang, X.C.; Bai, T.X.; Meng, X.; Ji, S.J.; Zhang, R.L.; Zheng, D.Y.; Yang, B.; Jiang, J.K.; Han, K.L.; Liu, F. Filling chlorine vacancy with bromine: A two-step hot-injection approach achieving defect-free hybrid halogen perovskite nanocrystals. *ACS Appl. Mater. Interfaces* **2022**, *14*, 18353–18359. [[CrossRef](#)]
19. Zeng, Y.T.; Li, Z.R.; Chang, S.P.; Ansay, A.; Wang, Z.H.; Huang, C.Y. Bright CsPbBr₃ perovskite nanocrystals with improved stability by in-situ Zn-doping. *Nanomaterials* **2022**, *12*, 759. [[CrossRef](#)]
20. Zhang, W.Z.; Li, X.; Peng, C.C.; Yang, F.; Lian, L.Y.; Guo, R.D.; Zhang, J.B.; Wang, L. CsPb(Br/Cl)(3) perovskite nanocrystals with bright blue emission synergistically modified by calcium halide and ammonium ion. *Nanomaterials* **2022**, *12*, 2026. [[CrossRef](#)]
21. Wang, J.; Xiong, L.; Bai, Y.; Chen, Z.J.; Zheng, Q.; Shi, Y.Y.; Zhang, C.; Jiang, G.C.; Li, Z.Q. Mn-doped perovskite nanocrystals for photocatalytic CO₂ reduction: Insight into the role of the charge carriers with prolonged lifetime. *Solar RRL* **2022**, *6*, 2200294. [[CrossRef](#)]
22. Li, N.; Chen, X.; Wang, J.; Liang, X.; Ma, L.; Jing, X.; Chen, D.L.; Li, Z. ZnSe nanorods–CsSnCl₃ perovskite heterojunction composite for photocatalytic CO₂ reduction. *ACS Nano* **2022**, *16*, 3332–3340. [[CrossRef](#)] [[PubMed](#)]
23. Hu, L.; Patterson, R.J.; Zhang, Z.; Hu, Y.; Li, D.; Chen, Z.; Yuan, L.; Teh, Z.L.; Gao, Y.; Conibeer, G.J.; et al. Enhanced optoelectronic performance in AgBiS₂ nanocrystals obtained via an improved amine-based synthesis route. *J. Mater. Chem. C* **2018**, *6*, 731–737. [[CrossRef](#)]
24. Oh, J.T.; Cho, H.; Bae, S.Y.; Lim, S.J.; Kang, J.; Jung, I.H.; Choi, H.; Kim, Y. Improved size distribution of AgBiS₂ colloidal nanocrystals by optimized synthetic route enhances photovoltaic performance. *Int. J. Energy Res.* **2020**, *44*, 11006–11014. [[CrossRef](#)]
25. Zafer Akgul, M.; Figueroba, A.; Pradhan, S.; Bi, Y.; Konstantatos, G. Low-cost RoHS compliant solution processed photovoltaics enabled by ambient condition synthesis of AgBiS₂ nanocrystals. *ACS Photon.* **2020**, *7*, 588–595. [[CrossRef](#)]
26. Liang, N.; Chen, W.; Dai, F.; Wu, X.; Zhang, W.; Li, Z.; Shen, J.; Huang, S.; He, Q.; Zai, J.; et al. Homogenously hexagonal prismatic AgBiS₂ nanocrystals: Controlled synthesis and application in quantum dot-sensitized solar cells. *Crystengcomm* **2015**, *17*, 1902–1905. [[CrossRef](#)]
27. Aldakov, D.; Lefrancois, A.; Reiss, P. Ternary and quaternary metal chalcogenide nanocrystals: Synthesis, properties and applications. *J. Mater. Chem. C* **2013**, *1*, 3756–3776. [[CrossRef](#)]
28. Burgues-Ceballos, I.; Wang, Y.; Akgul, M.Z.; Konstantatos, G. Colloidal AgBiS₂ nanocrystals with reduced recombination yield 6.4% power conversion efficiency in solution-processed solar cells. *Nano Energy* **2020**, *75*, 104961. [[CrossRef](#)]
29. Wang, Y.; Kavanagh, S.R.; Burgues-Ceballos, I.; Walsh, A.; Scanlon, D.; Konstantatos, G. Cation disorder engineering yields AgBiS₂ nanocrystals with enhanced optical absorption for efficient ultrathin solar cells. *Nat. Photon.* **2022**, *16*, 235–241. [[CrossRef](#)]
30. Bae, S.Y.; Oh, J.T.; Park, J.Y.; Ha, S.R.; Choi, J.; Choi, H.; Kim, Y. Improved eco-friendly photovoltaics based on stabilized AgBiS₂ nanocrystal inks. *Chem. Mater.* **2020**, *32*, 10007–10014. [[CrossRef](#)]
31. Gao, Y.; Peng, X. Photogenerated excitons in plain core CdSe nanocrystals with unity radiative decay in single channel: The effects of surface and ligands. *J. Am. Chem. Soc.* **2015**, *137*, 4230–4235. [[CrossRef](#)] [[PubMed](#)]
32. Zhang, F.; Huang, S.; Wang, P.; Chen, X.; Zhao, S.; Dong, Y.; Zhong, H. Colloidal synthesis of air-stable CH₃NH₃PbI₃ quantum dots by gaining chemical insight into the solvent effects. *Chem. Mater.* **2017**, *29*, 3793–3799. [[CrossRef](#)]
33. Oh, J.T.; Bae, S.Y.; Yang, J.; Ha, S.R.; Song, H.; Lee, C.B.; Shome, S.; Biswas, S.; Lee, H.M.; Seo, Y.H.; et al. Ultra-stable all-inorganic silver bismuth sulfide colloidal nanocrystal photovoltaics using pin type architecture. *J. Power Sources* **2021**, *514*, 230585. [[CrossRef](#)]
34. Chen, D.; Shivarudraiah, S.B.; Geng, P.; Ng, M.; Li, C.H.A.; Tewari, N.; Zou, X.; Wong, K.S.; Guo, L.; Halpert, J.E. Solution-processed, inverted AgBiS₂ nanocrystal solar cells. *ACS Appl. Mater. Interfaces* **2022**, *14*, 1634–1642. [[CrossRef](#)]
35. Kirchartz, T.; Deledalle, F.; Tuladhar, P.S.; Durrant, J.R.; Nelson, J. On the differences between dark and light ideality factor in polymer: Fullerene solar cells. *J. Phys. Chem. Lett.* **2013**, *4*, 2371–2376. [[CrossRef](#)]
36. Cowan, S.R.; Roy, A.; Heeger, A.J. Recombination in polymer-fullerene bulk heterojunction solar cells. *Phys. Rev. B* **2010**, *82*, 245207. [[CrossRef](#)]
37. Chen, C.; Qiu, X.; Ji, S.; Jia, C.; Ye, C. The synthesis of monodispersed AgBiS₂ quantum dots with a giant dielectric constant. *Crystengcomm* **2013**, *15*, 7644–7648. [[CrossRef](#)]
38. Huang, P.C.; Yang, W.C.; Lee, M.W. AgBiS₂ semiconductor-sensitized solar cells. *J. Phys. Chem. C* **2013**, *117*, 18308–18314. [[CrossRef](#)]
39. He, J.G.; Chen, J.; Yu, Y.; Zhang, L.; Zhang, G.Z.; Jiang, S.L.; Liu, W.; Song, H.S.; Tang, J. Effect of ligand passivation on morphology, optical and photoresponse properties of CdS colloidal quantum dots thin film. *J. Mater. Sci.-Mater. Electron.* **2014**, *25*, 1499–1504. [[CrossRef](#)]
40. Rath, T.; Novák, J.; Amenitsch, H.; Pein, A.; Maier, E.; Haas, W.; Hofer, F.; Trimmel, G. Real time X-ray scattering study of the formation of ZnS nanoparticles using synchrotron radiation. *Mater. Chem. Phys.* **2014**, *144*, 310–317. [[CrossRef](#)]
41. Liu, J.C.; Yu, H.Z.; Wu, Z.L.; Wang, W.L.; Peng, J.B.; Cao, Y. Size-tunable near-infrared PbS nanoparticles synthesized from lead carboxylate and sulfur with oleylamine as stabilizer. *Nanotechnology* **2008**, *19*, 345602. [[CrossRef](#)] [[PubMed](#)]
42. Yuan, B.; Tian, X.C.; Shaw, S.; Petersen, R.E.; Cademartiri, L. Sulfur in oleylamine as a powerful and versatile etchant for oxide, sulfide, and metal colloidal nanoparticles. *Phys. Status Solidi A* **2017**, *214*, 1600543. [[CrossRef](#)]
43. Ojha, G.P.; Pant, B.; Muthurasu, A.; Chae, S.H.; Park, S.J.; Kim, T.; Kim, H.Y. Three-dimensionally assembled manganese oxide ultrathin nanowires: Prospective electrode material for asymmetric supercapacitors. *Energy* **2019**, *188*, 116066. [[CrossRef](#)]

44. Nakazawa, T.; Kim, D.; Oshima, Y.; Sato, H.; Park, J.; Kim, H. Synthesis and application of AgBiS₂ and Ag₂S nanoinks for the production of IR photodetectors. *ACS Omega* **2021**, *6*, 20710–20718. [[CrossRef](#)] [[PubMed](#)]
45. Guin, S.N.; Biswas, K. Cation disorder and bond anharmonicity optimize the thermoelectric properties in kinetically stabilized rocksalt AgBiS₂ nanocrystals. *Chem. Mater.* **2013**, *25*, 3225–3231. [[CrossRef](#)]
46. Ju, M.G.; Dai, J.; Ma, L.; Zhou, Y.; Zeng, X.C. AgBiS₂ as a low-cost and eco-friendly all-inorganic photovoltaic material: Nanoscale morphology-property relationship. *Nanoscale Adv.* **2020**, *2*, 770–776. [[CrossRef](#)] [[PubMed](#)]
47. Pejova, B.; Grozdanov, I.; Nesheva, D.; Petrova, A. Size-dependent properties of sonochemically synthesized three-dimensional arrays of close-packed semiconducting AgBiS₂ quantum dots. *Chem. Mater.* **2008**, *20*, 2551–2565. [[CrossRef](#)]
48. Dolabella, S.; Borzi, A.; Dommann, A.; Neels, A. Lattice strain and defects analysis in nanostructured semiconductor materials and devices by high-resolution X-ray diffraction: Theoretical and practical aspects. *Small Methods* **2022**, *6*, 2100932. [[CrossRef](#)]
49. Nishimura, K.; Hirofani, D.; Kamarudin, M.A.; Shen, Q.; Toyoda, T.; Iikubo, S.; Minemoto, T.; Yoshino, K.; Hayase, S. Relationship between lattice strain and efficiency for Sn-perovskite solar cells. *ACS Appl. Mater. Interfaces* **2019**, *11*, 31105–31110. [[CrossRef](#)]
50. Li, X.P.; Huang, R.J.; Chen, C.; Li, T.; Gao, Y.J. Simultaneous conduction and valence band regulation of indium-based quantum dots for efficient H₂ photogeneration. *Nanomaterials* **2021**, *11*, 1115. [[CrossRef](#)]
51. Wang, Q.; Wang, J.; Wang, J.C.; Hu, X.; Bai, Y.; Zhong, X.; Li, Z. Coupling CsPbBr₃ quantum dots with covalent triazine frameworks for visible-light-driven CO₂ reduction. *ChemSusChem* **2021**, *14*, 1131–1139. [[CrossRef](#)] [[PubMed](#)]
52. Chang, J.; Oshima, T.; Hachiya, S.; Sato, K.; Toyoda, T.; Katayama, K.; Hayase, S.; Shen, Q. Uncovering the charge transfer and recombination mechanism in ZnS-coated PbS quantum dot sensitized solar cells. *Sol. Energy* **2015**, *122*, 307–313. [[CrossRef](#)]
53. Chang, J.; Zhang, S.; Wang, N.; Sun, Y.; Wei, Y.; Li, R.; Yi, C.; Wang, J.; Huang, W. Enhanced performance of red perovskite light-emitting diodes through the dimensional tailoring of perovskite multiple quantum wells. *J. Phys. Chem. Lett.* **2018**, *9*, 881–886. [[CrossRef](#)] [[PubMed](#)]
54. Amaral-Junior, J.C.; Mansur, A.A.P.; Carvalho, I.C.; Mansur, H.S. Tunable luminescence of Cu-In-S/ZnS quantum dots-polysaccharide nanohybrids by environmentally friendly synthesis for potential solar energy photoconversion applications. *Appl. Surf. Sci.* **2021**, *542*, 148701. [[CrossRef](#)]
55. Ma, Y.; Zhang, Y.; Liu, M.; Han, T.; Wang, Y.; Wang, X. Improving the performance of quantum dot sensitized solar cells by employing Zn doped CuInS₂ quantum dots. *Adv. Compos. Hybrid Mater.* **2022**, *5*, 402–409. [[CrossRef](#)]
56. Akgul, M.Z.; Konstantatos, G. AgBiSe₂ colloidal nanocrystals for use in solar cells. *ACS Appl. Nano Mater.* **2021**, *4*, 2887–2894. [[CrossRef](#)]
57. Ming, S.; Liu, X.; Zhang, W.; Xie, Q.; Wu, Y.; Chen, L.; Wang, H.Q. Eco-friendly and stable silver bismuth disulphide quantum dot solar cells via methyl acetate purification and modified ligand exchange. *J. Clean. Prod.* **2020**, *246*, 118966. [[CrossRef](#)]
58. Lee, D.H.; Condrate, R.A.; Lacourse, W.C. FTIR spectral characterization of thin film coatings of oleic acid on glasses—Part II—Coatings on glass from different media such as water, alcohol, benzene and air. *J. Mater. Sci.* **2000**, *35*, 4961–4970. [[CrossRef](#)]
59. Thomson, J.W.; Nagashima, K.; Macdonald, P.M.; Ozin, G.A. From sulfur–amine solutions to metal sulfide nanocrystals: Peering into the oleylamine–sulfur black box. *J. Am. Chem. Soc.* **2011**, *133*, 5036–5041. [[CrossRef](#)]
60. Williamson, G.K.; Hall, W.H. X-ray line broadening from fcc aluminium and wolfram L'elargissement des raies de rayons x obtenues des limailles d'aluminium et de tungsten Die verbreiterung der roentgeninterferenzlinien von aluminium- und wolframspaenen. *Acta Metall.* **1953**, *1*, 22–31. [[CrossRef](#)]